Estimation of high temperature phase equilibria in directionally solidified intermetallic Ti-45.9Al-8Nb alloy

Z. Gabalcová, J. Lapin*

Institute of Materials and Machine Mechanics, Slovak Academy of Sciences, Račianska 75, 831 02 Bratislava, Slovak Republic

Received 17 September 2007, received in revised form 22 October 2007, accepted 22 October 2007

Abstract

High temperature phase equilibria were studied in directionally solidified (DS) intermetallic Ti-45.9Al-8Nb (at.%) alloy by the means of quench during directional solidification (QDS) experiments, microstructure analysis and differential thermal analysis (DTA). During directional solidification at constant growth rates V ranging from 5.56×10^{-6} to 1.18×10^{-4} m s^{-1} and three measured temperature gradients in liquid at the solid-liquid interface G_L of 3.5×10^3, 5×10^3 and 8×10^3 K m^{-1} the primary solidification phase is identified to be β phase (Ti based solid solution with bcc crystal structure). The microstructural analysis of quenched mushy zones excluded formation of α phase (Ti based solid solution with hcp crystal structure) by a peritectic reaction during directional solidification. Experimentally determined phase transformation sequences L (liquid) $\rightarrow$ L + $\beta \rightarrow \beta \rightarrow \beta + \alpha$ and estimated high temperature phase stability are different from those resulting from thermodynamic calculations using Thermo-Calc software and TiAl database. Due to preferred [001] crystallographic orientation of the β dendrites, lamellar $\alpha_2(Ti_3Al)/\gamma(TiAl)$ boundaries in DS ingots are observed to be inclined at the angles of 0° and 45° to the growth direction.

K e y w o r d s: titanium aluminides, TiAl, crystal growth, phase transformations, microstructure

1. Introduction

In recent years multiphase TiAl-based intermetallic alloys [1–12] have been extensively studied as potential replacements for nickel-based superalloys [13–16], nickel [17–19] or iron [20–23] based intermetallic alloys and conventional titanium alloys [24, 25]. Depending on chemical composition and heat treatments, TiAl-based alloys exhibit four different types of microstructures: (i) near gamma, (ii) duplex, (iii) near lamellar, and (iv) fully lamellar [26–28]. The fully lamellar or nearly lamellar microstructure consisting of TiAl (γ phase) and a small volume fraction of Ti_3Al (α_2 phase), exhibits better creep resistance (apart from primary creep), higher fracture toughness and crack propagation resistance than duplex microstructures [29–32]. On the other hand, higher tensile strength, ductility and longer fatigue life are achieved for alloys with duplex microstructure [31].

A good combination of room temperature strength, ductility, toughness and creep strength can be achieved when the lamellar orientation is aligned parallel to the tensile direction [32–36]. As shown in recent studies [37–40], preferred lamellar orientation can be achieved by directional solidification techniques. The main difficulty of directional solidification is that the lamellar microstructure is not formed from the liquid but from the solid state by precipitation of γ lamellae in either a disordered α (Ti based solid solution with hexagonal crystal structure) or an ordered α_2-matrix following Blackburn crystallographic orientation relationships of $(0001)_{\alpha_2} \parallel \{111\}_\gamma$ and $\langle 11\bar{2}0\rangle_{\alpha_2} \parallel \langle 1\bar{1}0\rangle_\gamma$ [41]. Since the preferred growth direction of α dendrites is parallel to the [0001] crystallographic direction, the lamellar orientation is perpendicular to the growth direction. Hence, to achieve the required lamellar orientation parallel to ingot axis, the orientation of the high temperature

*Corresponding author: tel.: +421 2 49268290; fax: +421 2 44253301; e-mail address: ummslapi@savba.sk

α phase must first be controlled. One approach to achieve the required orientation is by seeding of the α phase in the alloys where: (1) α phase is the primary solidification phase, (2) nucleation of the primary β phase (Ti based solid solution with bcc crystal structure) can be suppressed and (3) α phase is the interdendritic phase and β phase is the primary solidification phase [40]. Another approach to achieve the required orientation of the α phase is without seeding by controlling the solidification path of alloys through appropriate alloying [42].

The aim of this paper is to estimate high temperature phase equilibria in directionally solidified (DS) intermetallic Ti-45.9Al-8Nb (at.%) alloy. Phase diagram of the studied alloy around the melting temperature is not clear and basic experimental data such as primary solidification phase, eventual occurrence of peritectic transformation and solidification interval is of great interest to justify theoretical thermodynamic calculations of phase equilibria for this system. The studied alloy has been selected as potential material for the investment casting of low-pressure turbine blades of aircraft engines and stationary gas turbines for power engineering [43]. In this alloy, the addition of 8 at.% of Nb improves high oxidation resistance and 45.9 at.% of Al guarantees grain refinement of the as-cast microstructures through massive transformation of the α phase to γ phase during quenching from single α phase field [44, 45].

2. Experimental procedure

The intermetallic alloy with the chemical composition Ti-45.9Al-8Nb (at.%) and oxygen content of 500 wtppm was supplied in the form of vacuum arc remelted cylindrical ingot with a diameter of 220 mm and a length of 60 mm. The ingot was cut to smaller blocks using electro spark machining, lathe machined to a diameter of 8 mm and length of 110 mm and directionally solidified in dense cylindrical Y_2O_3 moulds (purity of 99.5 %) with a diameter of 8/12 (inside/outside diameter) and length of 130 mm. Directional solidification was performed at constant growth rates V varying in the range from 5.56×10^{-6} to 1.18×10^{-4} m s^{-1} in a modified Bridgman-type apparatus described elsewhere [46]. Before directional solidification the vacuum chamber of the apparatus was evacuated to a pressure of 3 Pa, flushed with argon (purity 99.9995 %) six times and then backfilled with argon at a pressure of 10 kPa, which was held constant during melting and solidification. In order to bind oxygen traces in the argon atmosphere and absorbed on the furnace walls and avoid their effect on the contamination of DS ingots, granules of Ca (purity of 98.8 %) with total weight of 15 g were placed in a metallic container close to the ceramic mould and heated to a constant temperature of 753 K during each directional solidification. The alloy was heated to three different set-up temperatures T of 1923, 1953 and 1993 K. The heating rate was 0.37 K s^{-1} and the melt was stabilized at T for 300 s. In order to preserve the conditions at solid-liquid interface, after directional solidification to a constant length of 50 mm the ingots were quenched by a rapid displacement of the mould into the water-cooled crystallizer.

Temperature profiles and gradients in the ingots were measured by PtRh30-PtRh6 thermocouples with a diameter of 0.15 mm at three set-up temperatures of 1923, 1953 and 1993 K. The thermocouple wires were put into high-purity alumina capillaries with an outside diameter of 1.2 mm. In order to protect the thermocouples against a direct contact with the melt, the measurements were performed in protective one end closed alumina tube with a diameter of 1.5/3 mm (inside/outside diameter) and length of 600 mm. In order to position the protective tube precisely to longitudinal ingot axis, the ingot was cut longitudinally by electro spark machining and grooves parallel to its longitudinal axis were machined by grinding in both parts of the ingot. The assembled ingot with the protective tube was placed in Y_2O_3 mould, heated to a selected melt temperature at a heating rate of 0.37 K s^{-1} and stabilized at the melt temperature for 600 s before temperature measurements. The temperature was continuously monitored with ADAM-4018 analog input module and time-temperature data acquisition was performed by a computer. The temperature profiles were measured at two different positions of the ingots in the crystallizer of 0 and 30 mm at constant set-up temperatures in the furnace. It should be noted that the attempts to measure temperature changes in the ingots at various applied growth rates were not successful due to limited lifetime of the thermocouples (about 600 s).

The solidus and liquidus temperatures of the alloy were determined by differential thermal analysis (DTA) in alumina crucibles using alumina powder as the reference standard. The DTA specimens were cut from the as-received ingot by electro spark machining and lathe machined to cylinders with a diameter of 5 mm and length of 3 mm. The transformation temperatures were measured by PtRh30-PtRh6 thermocouple at a heating and cooling rate of 8.33×10^{-2} K s^{-1} under argon atmosphere.

Microstructural analysis was performed by optical microscopy (OM), scanning electron microscopy (SEM) and energy-dispersive spectrometry (EDS) on longitudinal and transversal sections of DS ingots. OM and SEM samples were prepared using standard metallographic techniques including grinding on SiC papers, polishing on diamond paste and etching in a reagent of 150 ml H_2O, 25 ml HNO_3 and 10 ml HF.

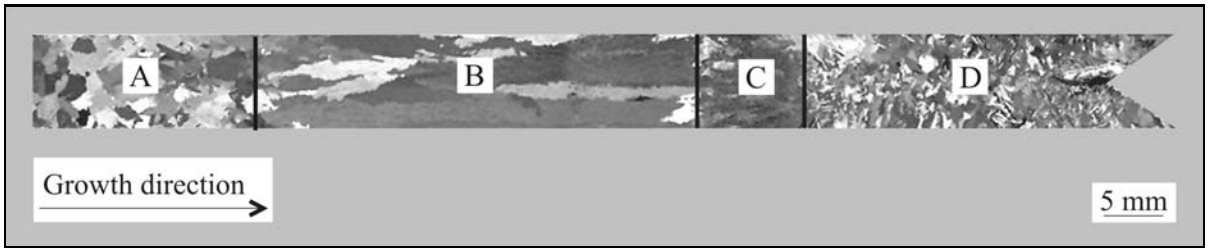

Fig. 1. OM showing macrostructure of longitudinal section of ingot after directional solidification at $V = 5.56 \times 10^{-5}$ m s^{-1} and $G_L = 5 \times 10^3$ K m^{-1} to a length of 50 mm followed by quenching. A – non-melted part of the ingot, B – DS part with columnar grain structure, C – mushy zone, D – quenched liquid.

3. Results

3.1. Analysis of quenched solid-liquid interfaces

Figure 1 shows an example of the typical macrostructure observed in quenched ingots after directional solidification to a length of 50 mm at constant growth rates V ranging from 5.56×10^{-6} to 1.18×10^{-4} m s^{-1} and three different temperatures T of 1923, 1953 and 1993 K. The macrostructure consists of non-melted part of the ingot with equiaxed grains (region A), DS part with columnar grains (region B), mushy zone (region C) and quenched liquid with equiaxed grains (region D). Analysis of microstructure in columnar grain region (region B) by the means of OM, SEM or backscattered SEM revealed high homogenization of the alloy. Low contrast resulting from the homogenization avoided identification of morphology of primary solidification phase. Therefore, the metallographic observations were focused on quenched solid-liquid interfaces and detailed analysis of the mushy zones (region C), which microstructure could be revealed by etching and studied by OM.

Figure 2 shows quenched solid-liquid interface with dendritic microstructure. Similar solid-liquid interfaces were observed in all ingots prepared by quench during directional solidification (QDS) experiments. The dendrites are oriented in a direction nearly parallel to the growth direction, which is identical with the longitudinal ingot axis. Figure 3 shows the typical microstructure of the dendrites in the mushy zone. As seen on transverse section in Fig. 3a, secondary dendrite arms are oriented at an angle of 90° to each other and form the typical "maltese cross". Besides well-developed secondary arms, tertiary dendrite arms orientated at an angle of 90° to the secondary arms can be also clearly identified. Four-fold symmetry of dendrites suggests a primary solidification phase with cubic crystal structure. Assuming the chemical composition of the studied alloy, β phase was the primary solidification phase during directional solidification. Figure 3b shows the morphology and orientation of the secondary dendrite arms on a longitudinal section at a distance of 2 mm from the dendrite tips. The absence of tertiary dendrite arms indicates fast coarsening process of the secondary arms within the mushy zone.

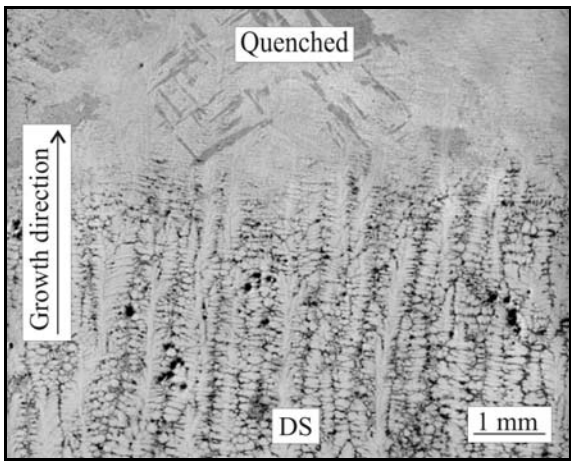

Fig. 2. OM showing morphology of quenched solid-liquid interface on a longitudinal section of the ingot prepared at $V = 5.56 \times 10^{-5}$ m s^{-1} and $G_L = 5 \times 10^3$ K m^{-1}. The growth direction, DS part and quenched liquid are indicated in the figure.

3.2. Differential thermal analysis

The precise measurements of liquidus T_L and solidus T_S temperatures were performed by DTA using heating cycles. Cooling DTA curves were not considered to be representative due to possible contamination of the alloy by oxygen and ceramic particles resulting from interactions between the melt and alumina crucible recently reported by Lapin et al. [46, 47]. Figure 4 shows an example of DTA heating curve and transformation temperatures T_L and T_S. As seen in this figure, solidification of the studied alloy starts at a liquidus temperature of $T_L = 1843$ K and is finalized at a solidus temperature of $T_S = 1778$ K. Freezing interval of the alloy $\Delta T = T_L - T_S = 65$ K is relatively large, which explains dendritic growth at all applied solidification parameters. Assuming large freezing interval, the growth of the studied alloy on a planar

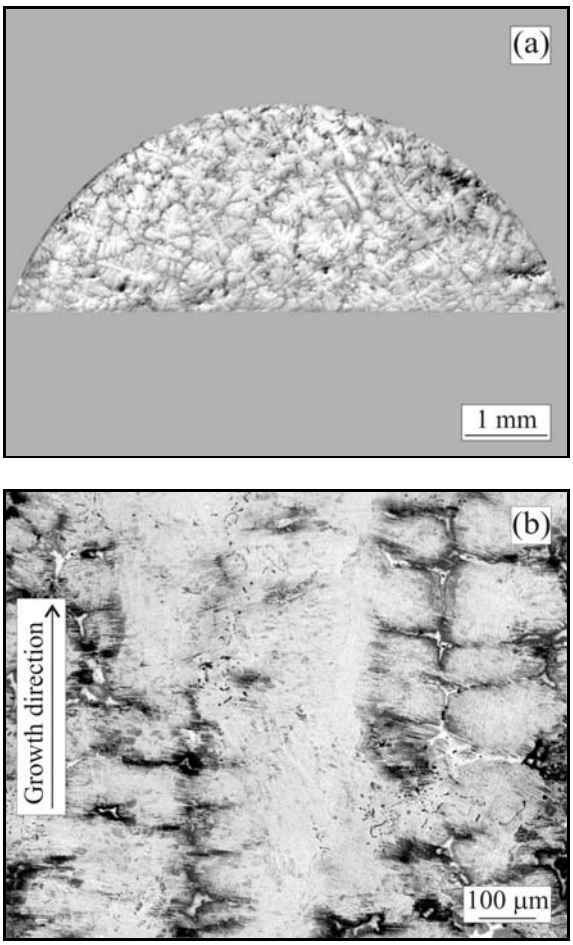

Fig. 3. OM showing morphology of dendrites in the mushy zone, $V = 2.78 \times 10^{-5}$ m s^{-1}: (a) transverse section at a position of 3 mm from the dendrite tips, $G_L = 3.5 \times 10^3$ K m^{-1}, (b) longitudinal section at a position of 2 mm from the dendrite tips, $G_L = 5 \times 10^3$ K m^{-1}.

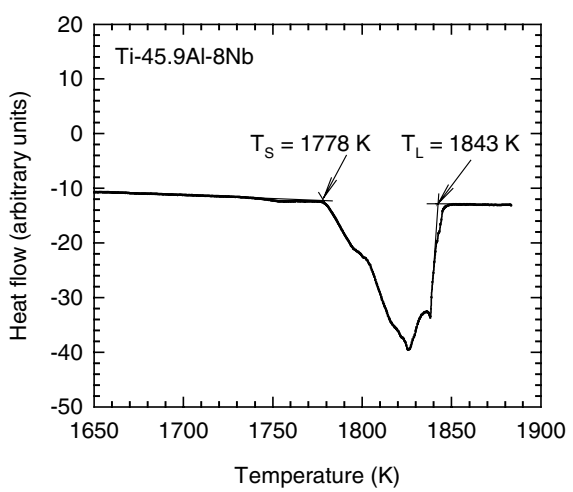

Fig. 4. DTA heating curve showing solidus T_S and liquidus T_L temperatures.

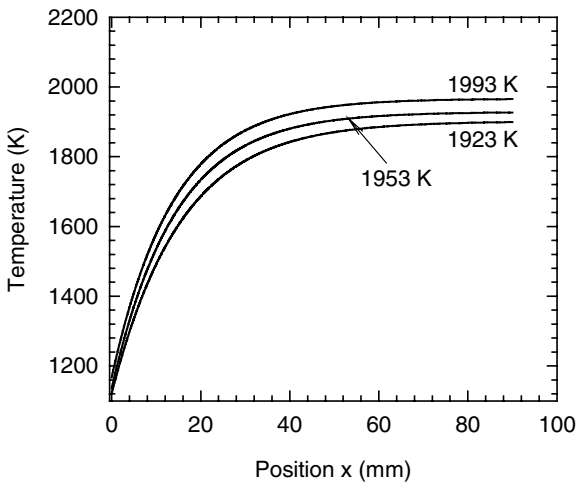

Fig. 5. Dependence of local temperature on the position x in the ingot. The set-up temperatures are indicated in the figure.

interface can be achieved at very low growth rates V and high temperature gradients in liquid at the solid-liquid interface G_L according to relationship in the form [48]

$$\frac{G_L}{V} \geq \frac{\Delta T}{D_L}, \tag{1}$$

where D_L is the diffusion coefficient in the liquid ($D_L = 2.8 \times 10^{-9}$ m^2 s^{-1} [49]). As a first estimate, assuming technically achievable temperature gradient in the directional solidification apparatus of $G_L = 8 \times 10^3$ K m^{-1} [46], maximum growth rate for a planar solid-liquid interface should not exceed 3.4×10^{-7} m s^{-1}. This maximum growth rate is of about one order of magnitude lower that the minimum growth rate used in the present study.

3.3. Measurements of temperature distribution and temperature gradients in liquid

In order to relate observed microstructures to local temperatures, measurements of temperature profiles were performed along longitudinal axis of the ingots. Figure 5 shows measured temperature distribution curves at three set-up temperatures ranging from 1923 to 1993 K. At all set-up temperatures, the ingot temperature increases continuously from the beginning of the ingot (non-melted part in contact with water cooled withdrawal rod) and reaches nearly constant value at a position of about 65 mm. The temperature gradients in liquid at the solid-liquid interface $G_L = \mathrm{d}T/\mathrm{d}x$ (x is the position in the ingot) were determined as a difference between a local temperature in the melt at a distance of 10 mm from the solid-liquid interface and the liquidus temperature of $T_L =$

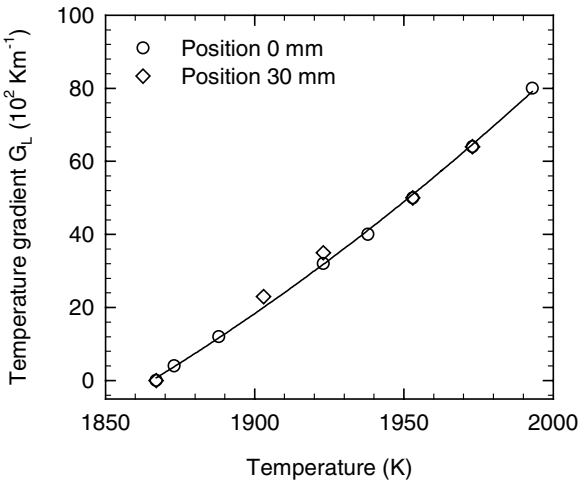

Fig. 6. Dependence of temperature gradient in liquid at the solid-liquid interface G_L on set-up temperature. Two different positions of the ingot in the crystallizer are indicated in the figure.

1843 K determined by DTA. Figure 6 shows dependence of temperature gradient G_L on the set-up temperature at two different positions of the ingot in the crystallizer. It is clear that the position of the ingot in the crystallizer has no effect on the temperature gradient G_L. The temperature gradient G_L depends only on the temperature and increases from 4×10^2 to 8×10^3 K m^{-1} with increasing set-up temperature. It should be noted that such stationary measurements of temperature gradient G_L do not include the effect of heat of fusion according to relationship [50]

$$K_S G_S = K_L G_L + \rho_S V L_v, \qquad (2)$$

where K_S and K_L are the thermal conductivities of the solid and liquid metal, respectively; G_S is the temperature gradient in solid at the solid-liquid interface, ρ_S is the density of solid metal and L_v is the heat of fusion. It is clear from Eq. (2) that the temperature gradients G_S and G_L are affected by increasing growth rate. As results from the measurements recently published by Jung et al. [51] for DS Ti-44Al (at.%) alloy, an increase of the growth rate from 2.5×10^{-5} to 1×10^{-4} m s^{-1} resulted in an increase of liquidus temperature from 1553 to 1557 K, increase of temperature gradient G_L from 1.4×10^3 to 1.6×10^3 K m^{-1} and variation in temperature gradient G_S from 2.3×10^3 to 2.6×10^3 K m^{-1} when measured at a distance of 10 mm from the solid-liquid interface. It should be also emphasized that these directional solidification experiments were performed in alumina moulds [51], which was proved to lead to alloy contamination [52]. Therefore, such measurements of temperature gradients were affected by superposition of two parameters: (i) dynamic solidification parameters connected with three different growth rates and (ii) various levels of alloy contamination resulting from different interaction time between the melt and the mould, which might affect phase transformation temperatures. Hence, the measured differences in temperature gradients resulting from the applied growth rates can be considered to be negligible assuming the applied methodology and accuracy of the measurements.

3.4. Estimation of high temperature phase equilibria

QDS experiments were used to estimate solidification path and correlate observed microstructures with local temperatures in the ingots. Figure 7 shows the typical microstructure of ingots prepared by QDS. Three regions with different type of microstructure can be clearly distinguished on longitudinal section of QDS ingot, as seen in Fig. 7a. In the region I, the microstructure consists of β dendrites and quenched interdendritic liquid, as shown in Fig. 7b. As reported by Zollinger et al. [53], during directional solidification of Ti-Al-Nb type of intermetallic alloys, Ti and Nb segregate into the dendrites and Al into interdendritic region. Local enrichment of interdendritic liquid by Al leads to formation of γ phase during quenching. Besides the γ phase, no other phase indicating peritectic type of reaction was found in the mushy zone. Due to thermodynamic instability, the high temperature β phase transforms to the α phase and residual β phase enriched by Nb forms a network within the dendrites during quenching (Fig. 7b). Detailed analysis by backscattered SEM shows that the α phase is also not stable and transforms to a lamellar $\alpha_2+\gamma$ microstructure. The fast transformation of the β phase to the α phase during quenching is the main reason why the primary solidification phase cannot be identified by a simple phase analysis of the as-grown ingots and other methods such as QDS experiments combined with metallographic analysis are required. Figure 7c shows very low contrast indicating high level of homogenization of the single β phase region II formed just below the mushy zone. As in the previous case, high temperature β phase is not stable and transforms to the α phase with very fine residual β during quenching. Detailed microstructure analysis revealed areas with fine lamellar $\alpha_2 + \gamma$ microstructure and single-phase regions, in which the α phase probably transformed to massive γ during quenching. Figure 7d shows basket weave type of microstructure observed in the region III. The microstructure consists of the α phase and coarse residual β phase. The α phase is found to be unstable and transforms to two types of microstructures: (i) lamellar $\alpha_2 + \gamma$ and (ii) probably massive γ.

In order to estimate temperature stability of different microstructures observed in QDS ingots, the

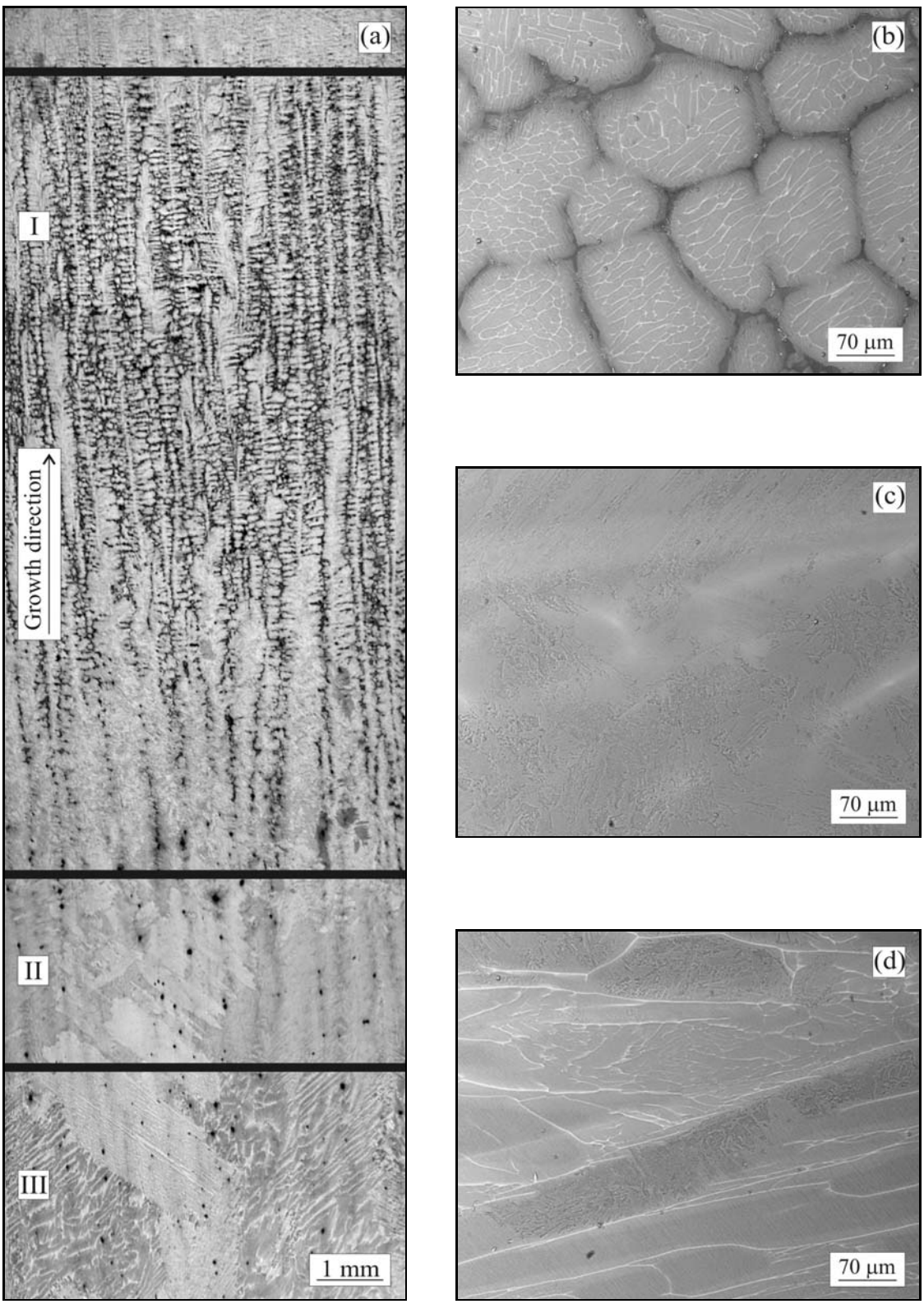

Fig. 7. Microstructure of longitudinal section of ingot prepared by quench during directional solidification (QDS) experiment, $V = 5.56 \times 10^{-5}$ m s^{-1} and $G_L = 3.5 \times 10^3$ K m^{-1}: (a) OM showing three microstructurally different regions marked as I, II and III, (b) backscattered SEM showing microstructure of the region I, (c) backscattered SEM showing microstructure of the region II, (d) backscattered SEM showing microstructure of the region III.

Table 1. Length of the β phase region, length of the mushy zone, solidus temperature and β phase decomposition temperature determined in QDS ingots prepared at five growth rates V and three temperature gradients G_L

Growth rate V (10^{-6} m s^{-1})	Temperature gradient in liquid G_L (10^3 K m^{-1})	Length of β phase region (mm)	Length of mushy zone (mm)	Solidus temperature (K)	β phase decomposition temperature (K)
5.6		2.4	9.2	1798	1788
13.9		2.9	10.9	1787	1768
27.8	3.5	2.7	12.6	1779	1759
55.6		2.8	11.9	1783	1765
118.0		2.7	11.8	1784	1764
5.6		1.0	8.5	1773	1761
13.9		1.1	8.4	1769	1756
27.8	5.0	0.9	7.8	1776	1765
55.6		1.2	8.3	1773	1756
118.0		0.8	6.8	1787	1776
5.6		1.0	5.3	1783	1769
13.9		1.2	7.0	1764	1742
27.8	8.0	1.2	7.0	1764	1748
55.6		1.1	7.1	1764	1748
118.0		0.7	6.0	1779	1769
Mean value	–	–	–	1778	1762

length of regions I and II was measured and related to local temperatures determined from the measured temperature profiles shown in Fig. 5. Table 1 summarizes the measured length of the mushy zone (region I) and single β phase (region II) and corresponding temperatures at five applied growth rates V and three temperature gradients G_L. It is clear that the length of the mushy zone and single β phase region decreases with increasing temperature gradient G_L. Assuming constant liquidus temperature of $T_L = 1843$ K, the solidus temperature is estimated to vary between 1764 and 1798 K and β phase decomposition temperature between 1742 and 1788 K. Assuming mean values, the solidus temperature is determined to be $T_S = 1778$ K, single β phase region is stable between 1762 and 1778 K and β phase decomposition to $\alpha+\beta$ occurs below 1762 K. The mean solidus temperature of 1778 K corresponds to that determined by DTA. High temperature phase stability for the studied alloy can be described by equation in the form

$$\begin{array}{ccccc} \mathrm{L} & \rightarrow & \mathrm{L}+\beta & \rightarrow & \beta \quad \rightarrow \beta+\alpha \\ T > 1843\ \mathrm{K} & & 1843\text{–}1778\ \mathrm{K} & & 1778\text{–}1762\ \mathrm{K} < 1762\ \mathrm{K} \end{array} \quad (3)$$

Assuming a good agreement between the solidus temperature determined by DTA and QDS experiments, the precision of phase transformation temperature measurements by QDS method is estimated to be about ± 10 K. Hence, this method seems to be very useful to provide first input data for thermodynamic calculations of phase diagrams.

4. Discussion

4.1. Effect of primary solidification phase on lamellar orientation

As shown by Yamaguchi et al. [40], lamellar orientation in DS ingots depends on primary solidification phase and its crystallographic orientation to the ingot axis. During directional growth in a positive temperature gradient due to the anisotropy of properties such as solid-liquid interface energy and growth kinetics, the dendrites grow in crystallographic direction, which is the closest to the heat flow direction [54]. In the case of the β primary solidification phase, the dendrites grow in [001] crystallographic direction, which is nearly parallel to the longitudinal ingot axis, as seen in Fig. 2. Such preferred crystallographic growth direction of the β phase with bcc crystal structure determines growth directions of the {011} planes, which grow with an angle of 0° or 45° to the growth direction. When the β phase transforms to the α phase, the crystallographic orientation relationship $(110)_\beta \parallel (0001)_\alpha$ is maintained between coexisting phases [51]. Since the γ lamellae precipitate from the parent α phase following Blackburn crystallographic orientation relationships of $(0001)_{\alpha_2} \parallel \{111\}_\gamma$, it makes the lamellar boundary inclined at an angle of 0° or 45° to the growth direction, as schematically shown in Fig. 8. Figure 9 shows orientation of lamellae to the growth direction in DS ingot. It is clear that bimodal lamellar orientation with the angle close

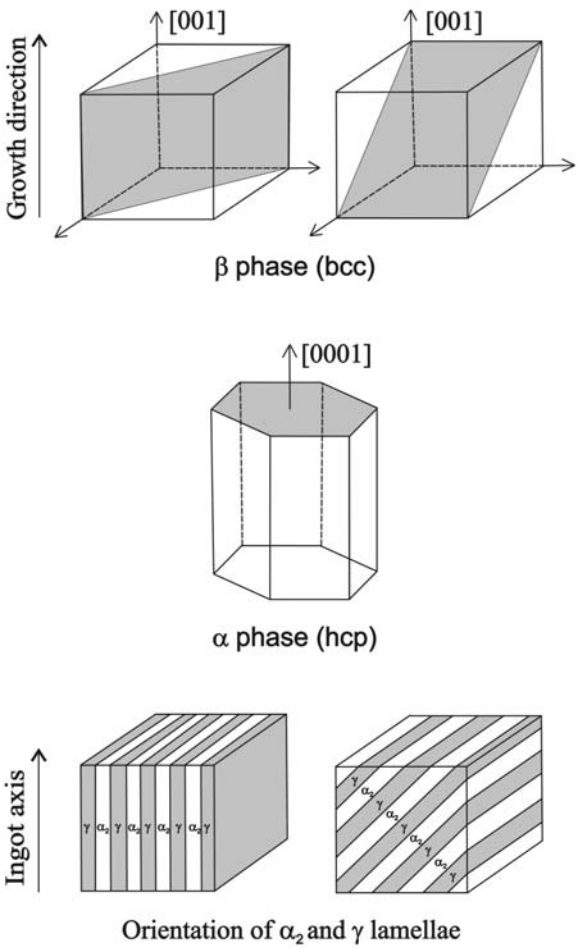

Fig. 8. Schema showing [001] crystallographic growth direction of the β phase with orientation of {110} crystallographic planes (grey color), orientation of (0001) plane (grey color) in the α phase and resulting two possible orientation variants of $\alpha_2 + \gamma$ lamellae in DS ingot.

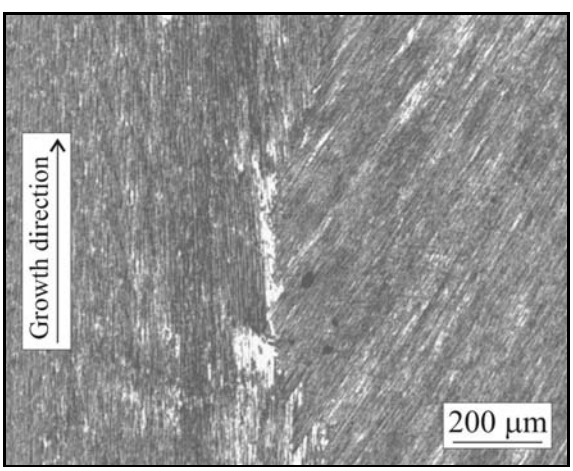

Fig. 9. OM showing lamellar orientation in DS ingot prepared at $V = 5.56 \times 10^{-5}$ m s^{-1} and $G_L = 8 \times 10^3$ K m^{-1}.

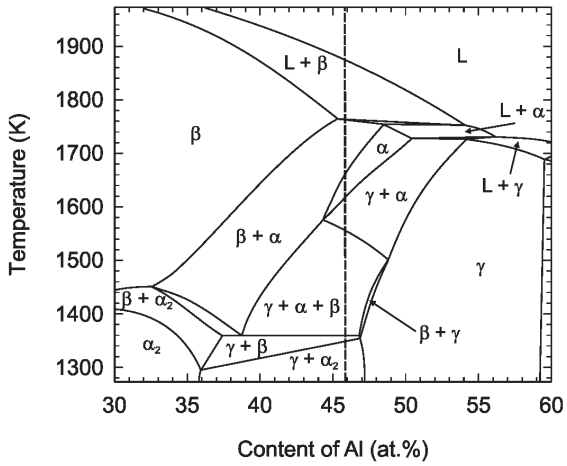

Fig. 10. Calculated quasi-binary phase diagram for ternary Ti-Al-Nb alloys with 8 at.% Nb. The chemical composition of the studied alloy is indicated in the figure.

to 0° in one grain and to 45° in the second grain is formed during cooling of the ingots in the temperature gradient of the furnace. Such post-solidification microstructure also gives clear evidence that the β phase was the primary solidification phase during directional solidification of Ti-45.9Al-8Nb (at.%) alloy. As shown by Lapin et al. [44], the lamellae grow with the angle of 90° to the growth direction in alloys with α primary solidification phase. The α solidification can be achieved by appropriate alloying or by oxygen contamination of alloys with β primary solidification phase (oxygen content higher than about 4800 wtppm) [55].

4.2. High temperature phase equilibria

Figure 10 shows quasi binary phase diagram for ternary Ti-Al-Nb alloys with 8 at.% Nb determined by Thermo-Calc software and TiAl database [56]. According to this phase diagram, equilibrium solidification of Ti-45.9Al-8Nb (at.%) leads to the following solidification sequences:

$$\mathrm{L} \rightarrow \mathrm{L} + \beta \rightarrow \mathrm{L} + \beta + \alpha \rightarrow \beta + \alpha \rightarrow \alpha \rightarrow \gamma + \alpha \rightarrow \\ \rightarrow \gamma + \alpha + \beta \rightarrow \gamma + \beta \rightarrow \gamma + \alpha_2. \qquad (4)$$

There are several main differences between the solidification path determined experimentally using QDS experiments and DTA and that calculated by thermodynamic software. Firstly, the calculated liquidus temperature of $T_L = 1878$ K is by 35 K higher than that resulting from DTA. The calculated solidus temperature (peritectic temperature) of $T_S = 1768$ K is by about 10 K lower than that resulting from DTA or QDS experiments. The freezing interval of

$\Delta T = 110$ K is by 45 K larger than that measured by DTA. Concerning the solidification sequences, the calculated phase diagram clearly indicates peritectic reaction L + $\beta + \alpha$ at 1768 K leading to formation of $\beta + \alpha$ microstructure. Experimental observations using QDS experiments clearly showed that no peritectic phase is formed during directional solidification and single β phase region is achieved just below the mushy zone. From this point of view, the calculated high temperature phase equilibria are misleading and the phase diagram does not fully correspond to experimentally observed solidification path. Hence, QDS experiments can be considered as useful approximate experimental tool to verify thermodynamic calculations for intermetallic systems, in which high temperature phases pass through several solid phase transformations resulting in fast alloy homogenization.

5. Conclusions

The investigation of high temperature phase equlibria in DS Ti-45.9Al-8Nb (at.%) alloy suggests the following conclusions:

1. During directional solidification at constant growth rates ranging from 5.56×10^{-6} to 1.18×10^{-4} m s^{-1} and temperature gradients in liquid at the solid-liquid interface from 3.5×10^3 to 8×10^3 K m^{-1} the primary solidification phase is identified to be dendritic β phase with bcc crystal structure.

2. The β dendrites grow in [001] crystallographic direction, which is nearly parallel to the growth direction and ingot axis. During solid phase transformations of the β phase to final lamellar $\alpha_2 + \gamma$ microstructure the preferred crystallographic orientation of the β phase results in lamellar boundaries inclined at the angles of 0° and 45° to the growth direction.

3. Microstructural analysis of the mushy zones excluded a peritectic reaction during near equilibrium directional solidification of the studied alloy. Experimentally determined phase transformation sequences L $\rightarrow$ L + $\beta \rightarrow \beta \rightarrow \beta + \alpha$ and estimated high temperature phase stability are different from those resulting from thermodynamic calculations using Thermo-Calc software and TiAl database.

Acknowledgements

This work was financially supported by EU Integrated Project IMPRESS "Intermetallic Materials Processing in Relation to Earth and Space Solidification" under the contract No. NMP3-CT-2004-500635. One of the authors (J. Lapin) would like to acknowledge the financial support of the Slovak Grant Agency for Science under the contract VEGA 2/7085/27.

References

[1] NAZMY, M.—LUPINC, V.: In: Materials for Advanced Power Engineering 2002. Eds.: Lecomte-Beckers, J., Carton, J. M., Schubert, F., Ennis, P. J. Forschungszentrum Jülich GmbH, Vol. 21, Part I, 2002, p. 43.
[2] HARDING, R. A.: Kovove Mater., *42*, 2004, p. 225.
[3] SANIN, V.—YUKHVID, V.—SYTSCHEV, A.—ANDREEV, D.: Kovove Mater., *44*, 2006, p. 49.
[4] LAPIN, J.: Kovove Mater., *43*, 2005, p. 81.
[5] LAPIN, J.—GABALCOVÁ, Z.—BAJANA, O.—DALOZ, D.: Kovove Mater., *44*, 2006, p. 297.
[6] CHENG, T. T.—LORETTO, M. H.: Acta Mater., *46*, 1998, p. 4801.
[7] LAPIN, J.: Kovove Mater., *44*, 2006, p. 57.
[8] ORLOVÁ, A.—KUCHAŘOVÁ, K.—DLOUHÝ, A.: Kovove Mater., *43*, 2005, p. 55.
[9] LAPIN, J.: Intermetallics, *14*, 2006, p. 115.
[10] KISHIDA, K.—JOHNSON, D. R.—MASUDA, Y.—UMEDA, H.—INUI, H.—YAMAGUCHI, M.: Intermetallics, *6*, 1998, p. 679.
[11] LAPIN, J.—NAZMY, M.: Mater. Sci. Eng. A, *380*, 2004, p. 298.
[12] RECINA, V.—LUNDSTRÖM, D.—KARLSSON, B.: Metall. Mater. Trans., *33A*, 2002, p. 2869.
[13] LUKÁŠ, P.—ČADEK, J.—KUNZ, L.—SVOBODA, M.—KLUSÁK, J.: Kovove Mater., *43*, 2005, p. 5.
[14] ROGANTE, M.—ŠAROUN, J.—STRUNZ, P.—CESCHINI, G. F.—RYUKHTIN, V.—LUKÁŠ, P.—MARINČÁK, V.: Kovove Mater., *43*, 2005, p. 371.
[15] ZRNÍK, J.—SEMEŇAK, J.—HORŇAK, P.—VRCHOVINSKÝ, V.: Kovove Mater., *43*, 2005, p. 93.
[16] KUNZ, L.—LUKÁŠ, P.—MINTÁCH, R.—HRBÁČEK, K.: Kovove Mater., *44*, 2006, p. 275.
[17] LAPIN, J.—BAJANA, O.: Kovove Mater., *43*, 2005, p. 169.
[18] LAPIN, J.—MAREČEK, J.—KURSA, M.: Kovove Mater., *44*, 2006, p. 1.
[19] LAPIN, J.: Intermetallics, *14*, 2006, p. 1417.
[20] PRAHL, J.—HAUŠILD, P.—KARLÍK, M.—CRENN, J. F.: Kovove Mater., *43*, 2005, p. 134.
[21] KRATOCHVÍL, P.—SCHINDLER, I.—HANUS, P.: Kovove Mater., *44*, 2006, p. 321.
[22] KRATOCHVÍL, P.—MÁLEK, P.—PEŠIČKA, J.—HAKL, J.—VLASÁK, T.—HANUS, P.: Kovove Mater., *44*, 2006, p. 185.
[23] PRAHL, J.—HAUŠILD, P.—KARLÍK, M.—CRENN, J. F.: Kovove Mater., *44*, 2006, p. 134.
[24] VOJTĚCH, D.—ČÍŽOVÁ, H.—MAIXNER, J.: Kovove Mater., *43*, 2005, p. 317.
[25] LEYENS, C.—PETERS, M.: Titanium and Titanium Alloys – Fundamentals and Applications. Weinheim, Wiley-VCH Verlag GmbH & Co. KgaA 2005.
[26] GIL, I.—MUÑOZ-MORRIS, M. A.—MORRIS, D. G.: Intermetallics, *9*, 2001, p. 373.
[27] RECINA, V.—AHLSTRÖM, J.—KARLSSON, B.: Mater. Charact., *38*, 1997, p. 287.
[28] YIN, W. M.—LUPINC, V.—BATTEZZATI, L.: Mater. Sci. Eng. A, *239–240*, 1997, p. 713.
[29] NAKAMURA, M.—NOBUKI, M.—TANABE, T.—KUMAGAI, T.—MUTOH, I.—ABE, E.: Intermetallics, *6*, 1998, p. 637.

[30] LAPIN, J.—KLIMOVÁ, A.: Kovove Mater., *41*, 2003, p. 1.
[31] APPEL, F.—WAGNER, R.: Mater. Sci. Eng. R, *R22*, 1998, p. 187.
[32] RECINA, V.—KARLSSON, B.: Mater. Sci. Techn., *15*, 1999, p. 57.
[33] YAMAGUCHI, M.—INUI, H.—YOKOSHIMA, S.—KISHIDA, K.—JOHNSON, D. R.: Mater Sci Eng A., *213*, 1996, p. 25.
[34] CHEN, W. R.—TRIANTAFILLOU, J.—BEDDOES, J.—ZHAO, L.: Intermetallics, *7*, 1999, p. 171.
[35] KISHIDA, K.—JOHNSON, D. R.—MASUDA, Y.—UMEDA, H.—INUI, H.—YAMAGUCHI, M.: Intermetallics, *6*, 1998, p. 679.
[36] KISHIDA, K.—INUI, H.—YAMAGUCHI, M.: Intermetallics, *7*, 1999, p. 1131.
[37] KIM, S. E.—LEE, Y. T.—OH, M. H.—INUI, H.—YAMAGUCHI, M.: Intermetallics, *8*, 2000, p. 399.
[38] JOHNSON, D. R.—INUI, H.—YAMAGUCHI, M.: Intermetallics, *6*, 1998, p. 647.
[39] LEE, H. N.—JOHNSON, D. R.—INUI, H.—OH, M. H.—WEE, D. M.—YAMAGUCHI, M.: Acta Mater., *48*, 2000, p. 3221.
[40] YAMAGUCHI, M.—JOHSON, D. R.—LEE, H. N.—INUI, H.: Intermetallics, *8*, 2000, p. 511.
[41] INUI, H.—NAKAMURA, A.—OH, M. H.—YAMAGUCHI, M.: Ultramicroscopy, *39*, 1991, p. 268.
[42] JOHNSON, D. R.—CHIHARA, K.—INUI, H.—YAMAGUCHI, M.: Acta Mater., *46*, 1998, p. 6529.
[43] JARVIS, D. J.—VOSS, D.: Mat. Sci. Eng. A, *413–414*, 2005, p. 583.
[44] HUANG, A.—HU, D.—WU, X.—LORETTO, M. H.: Intermetallics, *15*, 2007, p. 1147.
[45] HU, D.—HUANG, A. J.—WU, X.: Intermetallics, *15*, 2007, p. 327.
[46] LAPIN, J.—ONDRÚŠ, Ľ.—NAZMY, M.: Intermetallics, *10*, 2002, p. 1019.
[47] LAPIN, J.—ONDRÚŠ, Ľ.—BAJANA, O.: Mater. Sci. Eng. A, *360*, 2003, p. 85.
[48] TRIVEDI, R.—KURZ, W.: Metall. Trans. A, *21A*, 1990, p. 1311.
[49] LIU, Y.—YANG, G.—ZHOU, Y.: J. Cryst. Growth, *240*, 2002, p. 603.
[50] FLEMINGS, M. C.: Solidification Processing. McGraw-Hill, Inc. 1974, p. 3.
[51] JUNG, I. S.—KIM, M. C.—LEE, J. H.—OH, M. H.—WEE, D. M.: Intermetallics, *7*, 1999, p. 1247.
[52] LAPIN, J.—ONDRÚŠ, Ľ.: Kovove Mater., *40*, 2002, p. 161.
[53] ZOLLINGER, J.—DALOZ, D.—COMBEAU, H.—LAPIN, J.: In: Proceedings on the 5^{th} Decennial International Conference on Solidification Processing. Ed.: Jones, H. The University of Sheffield, ISBN-10:0-9522507-4-8, 2007, p. 282.
[54] KURZ, W.—FISHER, D. J.: Fundamentals of Solidification. Aedermannsdorf, Stwitzerland, Trans Tech Publications 1984, p. 70.
[55] ZOLLINGER, J.—LAPIN, J.—DALOZ, D.—COMBEAU, H.: Intermetallics, *15*, 2007, p. 1343.
[56] SAUNDERS, N.: TiAl data, thermodynamic database for calculation of phase equilibria in multicomponent TiAl alloys. Guilford, Thermothech Ltd. Surrey Technology Centre 2007.